Eur. Phys. J. A **6**, 451–461 (1999)

THE EUROPEAN PHYSICAL JOURNAL A

The E1 and E2 capture amplitudes in $^{12}C(\alpha,\gamma_0)^{16}O$

G. Roters, C. Rolfs, F. Strieder, H.P. Trautvetter

Institut für Physik mit Ionenstrahlen, Ruhr-Universität Bochum, Bochum, Germany

Received: 23 August 1999

Communicated by B. Povh

Abstract. Excitation functions of the γ_o capture transition in $^{12}C(\alpha,\gamma)^{16}O$ at $\theta_\gamma = 90°$ were obtained using a $4 \times 4''$ BGO crystal in close geometry ($E = 0.94$ to 3.39 MeV) and a $2 \times 2''$ BGO crystal in far geometry ($E = 1.69$ to 3.29 MeV), where the study of the reaction was initiated in inverse kinematics involving a windowless gas target. The small crystal detected essentially the $E1$ multipole component in the γ_0 capture transition, while the large crystal observed approximately the angle-integrated sum of the $E1$ and $E2$ multipole components. Analysis of the two data sets together with data from previous work provided strong evidence that both multipoles are of equal importance at the relevant stellar energy $E_0 = 0.3$ MeV.

1 Introduction

The capture reaction $^{12}C(\alpha,\gamma)^{16}O$ ($Q = 7.16$ MeV) takes place in the helium burning of Red Giants [1] and represents a key reaction of nuclear astrophysics. The cross section at the relevant Gamow energy, $E_0 = 0.3$ MeV (all energies are given in the center-of-mass system, except where quoted differently), determines not only the nucleosynthesis of elements up to the iron region but also the subsequent evolution of massive stars, the dynamics of a supernova, and the kind of remnant after a supernova explosion. For definitive calculations, the cross section $\sigma(E_0)$ must be known with a precision of at least 10%. In spite of tremendous experimental efforts over nearly 30 years, one is still far from this goal. Since $\sigma(E_0) \approx 10^{-17}$ b is far too small for direct measurement using available techniques, the measured cross sections at higher energies must be extrapolated to E_0.

Originally, $\sigma(E_0)$ was assumed to be dominated by the capture process into the ^{16}O ground state with an $E1$ amplitude arising from the low-energy tail of a broad $J^\pi = 1^-$ resonance at $E_R = 2.42$ MeV and the high-energy tail of a $J^\pi = 1^-$ subthreshold resonance at $E_R = -45$ keV including interference effects between both $E1$ sources. The first $^{12}C(\alpha,\gamma_0)^{16}O$ measurements [2,3] revealed a constructive interference at energies between the two resonances. The reaction was studied also in inverse kinematics [4], $^4He(^{12}C,\gamma_0)^{16}O$: the data suggested an $E2$ capture amplitude of the same order as the $E1$ capture amplitude at E_0, where the major $E2$ source is a $J^\pi = 2^+$ subthreshold resonance at $E_R = -245$ keV. Subsequent measurements of γ_0 angular distributions [5,7] supported this suggestion. The γ_0 capture transitions were studied also in coincidence with the ^{16}O recoil nuclides [6]. It was also found [4,5] that contributions of cascade transitions via the $E_x = 6.92$ and 7.12 MeV excited states in ^{16}O may not be negligible in the final $\sigma(E_0)$ value. The analysis and extrapolation of the dominant $E1$ and $E2$ γ_0 capture transitions depend critically on the reduced α widths of the $E_R = -45$ and -245 keV subthreshold resonances. Values for these widths were inferred from elastic-scattering data [9], the β-delayed α spectrum of ^{16}N [10,11], and α-transfer reactions [12,13]. In spite of enormous experimental difficulties, the overall agreement of the $E1$ and $E2$ γ_0-ray data appears to be satisfactory. However, a closer inspection reveals some differences among the data sets that are crucial because even small discrepancies in the measured cross sections can lead to major differences in the extrapolations. The present differences and statistical errors of the available data are too large at energies below and above the $E_R = 2.42$ MeV resonance to allow an extrapolation with the above precision.

To improve the situation, we have initiated the study of the reaction in inverse kinematics and observed the γ_0 capture transition at $\theta_\gamma = 90°$ using a $2 \times 2''$ BGO crystal (in short: $2''$BGO) in far geometry and a $4 \times 4''$ BGO crystal (in short: $4''$BGO) in close geometry: the $2''$BGO detected essentially the $E1$ multipole (angular distributions: $W_{E1}(\theta_\gamma) \propto \sin^2\theta_\gamma$ and $W_{E2}(\theta_\gamma) \propto \sin^2\theta_\gamma \cos^2\theta_\gamma$), while the $4''$BGO observed approximately the angle-integrated sum of the $E1$ and $E2$ multipoles.

2 Equipment and setup

The 4 MV Dynamitron tandem accelerator at the Ruhr-Universität Bochum provided a ^{12}C ion beam over the energy range $E_{lab} = 4.0$ to 15.5 MeV with a particle current of up to 20 μA at the target. Other ion beams (^{11}B, ^{15}N, and ^{16}O) were also provided for calibration purposes [14]. The energy calibration of the analysing magnet has been carried out previously over a wide magnetic field range [15] and resulted in a precision of heavy-ion beam energies of 4 parts in 10^4, which is sufficient for the requirements of the present work. The energy spread for ^{12}C ions was found [15] to be $\Delta E_{lab} = 2.8(1+q)$ keV at $E_{lab} = 10.5$ MeV, where q is the selected charge state.

A windowless gas-target system with five pumping stages was used, as described previously [15]. Briefly, the pumping stages (Fig. 1) consist of Roots blowers (e.g. WS2000, pumping speed = 2000 m^3/h) and turbo pumps (e.g. TV1500, pumping speed = 1500 l/s). The beam enters a disc-shaped target chamber ($\Phi = 20$ cm diameter, 3 cm height; central pipe of 2 cm diameter) through six apertures of high gas-flow impedance (A to F, with diameters Φ given in Fig. 1) and is stopped in a Faraday cup (surrounded by 0.5 m thick paraffin blocks) 7 m from the center of the chamber, with a 1.5 m thick concrete wall between the Faraday cup and the target chamber. The chamber has several ports radiating from its center, which is at a distance $z = 108 \pm 3$ mm from the center of aperture A ($\Phi = 6$ mm). These ports are used for several purposes (Fig. 1). The gas pressure in the target chamber was measured with a Baratron capacitance manometer to an accuracy of 4%. This measurement is absolute and independent of the gas used. For ^{4}He gas (99.9999% chemical purity) of $p = 9.1$ Torr pressure in the target chamber (this pressure was always used, except where quoted differently), the five-stage pumping system reduced the pressure to 0.10 and 1×10^{-6} Torr in the regions between the apertures A and B and E and F, respectively. A similar pressure reduction was observed for other p values and other target gases.

The main pressure drop occurs across the entrance aperture A of the target chamber. At the center of the target chamber, the gas pressure is essentially unmodified by the gas flow through aperture A, and the geometrically extended target zone is characterized by a nearly static gas pressure [14]. However, in determining the gas temperature one must include beam-heating effects in the gas, which may raise the local temperature along the beam path. The influence of intense ion beams on the densities of quasi-static gas targets was found [16] to depend on the dissipated power in the gas. In the present work, the effects on the gas density are less than 1% and were neglected in the analyses.

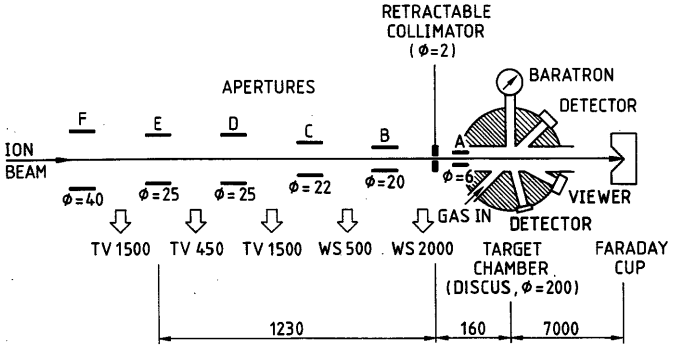

Fig. 1. Schematic of relevant parts of the gas-target system in side view. The quoted values of lengths and diameters are in mm

Due to the relatively large diameters of the apertures (chosen to minimize beam-induced background, Sect. 3.5), the ion-beam optics was defined by a retractable collimator ($\Phi = 2$ mm) placed – with a 0.1 mm reproducibility – on the beam axis in front of aperture A (Fig. 1). The collimator together with aperture E defined the angle of the incident beam to better than 0.6°. During the course of the experiments, the ion-beam optics was checked about every 3 hours.

The yield of the elastically scattered ^{4}He recoils was observed in Si surface-barrier detectors installed at the 45° and 75° ports of the target chamber. Each detector was collimated with an aperture (facing the detectors: $\Phi = 1.01$ mm for $\theta_{lab} = 45°$ and $\Phi = 0.70$ mm for $\theta_{lab} = 75°$) at a distance $d = 171$ mm from the center of the chamber and with a slit of width $s = 0.30$ mm placed at a distance $f = 145$ mm from the aperture. The geometry defined the effective target length seen by the detectors and their solid angle as $l_{effp}\Omega_{lab} = \pi r^2 s(fd\sin\theta_{lab})^{-1} = 14 \times 10^{-6}$ and 4.8×10^{-6} mm-sr for the 45° and 75° detectors, respectively. The geometry defined the detection angle to a precision $\Delta\theta_{lab} = 0.5°$. The elastic-scattering yield was used to monitor the product of beam intensity and target density as well as possible contaminants in both [14].

For γ-ray spectroscopy, a 2″BGO and a 4″BGO were used since they have a higher detection efficiency (about a factor 3) compared to NaI crystals of the same size. The BGO crystals were placed at $\theta_\gamma = 90°$ viewing the center of the target chamber (Fig. 2), where a 10 cm thick lead shield defined the effective target length $l_{eff\gamma}$ seen by each crystal. The 4″BGO had an energy resolution of 17% at $E_\gamma = 1.27$ MeV and was placed in close geometry ($d_\gamma = 4.0$ cm distance from the beam axis to its front face), while the 2″BGO was placed in far geometry ($d_\gamma = 24.5$ cm, energy resolution = 7%). The background due to high-energy γ rays and thermal neutron capture (created by cosmic rays) was minimized using a 10 cm thick lead shield and a 1 mm thick cadmium sheet, both surrounding completely the crystals: the passive shielding. The active shielding against muons consisted of plastic scintillators (type NE102A, 3 cm thickness): two scintillators (each of 1×1 m^2 area) were placed above the crystals (not shown in Fig. 2) and three scintillators (each of 0.5×1 m^2 area) were placed on the sides of the crystals (Fig. 2). Coincidence events between the crystals and the scintillators were rejected.

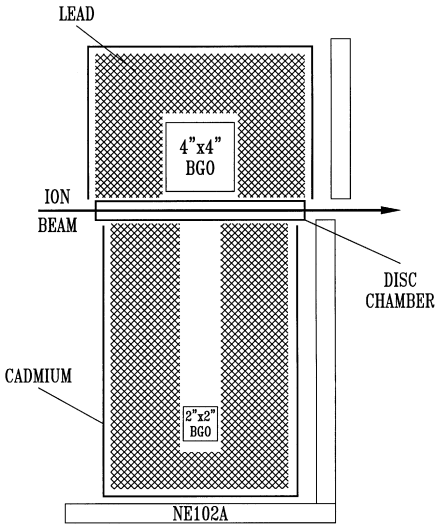

Fig. 2. Top view of the setup involving a $2 \times 2''$ BGO and a $4 \times 4''$ BGO surrounded by passive and active shieldings against background events, mainly due to cosmic rays. Not shown are the two plastic scintillators (NE102A, each of 1×1 m^2 area) placed above the crystals

3 Experimental procedures

3.1 Effective target length and relative detector efficiency

As just discussed, the effective target length $l_{eff\gamma}$ seen by each BGO was defined by the lead shield. For $E_\gamma = 1.27$ MeV, $l_{eff\gamma}$ was determined by moving a ^{22}Na source along the beam axis, in steps of 1 cm. The resulting response functions for the $4''$BGO and $2''$BGO (Fig. 3) led to respective lengths $l_{eff\gamma} = 13.0 \pm 0.5$ and 7.0 ± 0.3 cm, in good agreement with GEANT simulations [14,17]: $l_{eff\gamma} = 12.4 \pm 0.5$ and 7.0 ± 0.3 cm. The GEANT simulations [14] (in short: GEANT) were used also to determine $l_{eff\gamma}$ for γ-ray energies relevant to the ^{4}He(^{12}C,γ_0)^{16}O studies: e.g., $l_{eff\gamma} = 13.0 \pm 0.5$ cm for the $4''$BGO at $E_\gamma = 9.5$ MeV.

The observed response functions were integrated over the distance along the beam axis to obtain the efficiency of the crystals for an extended γ-ray source. In the analysis discussed in Sect. 4.3, only the efficiency of the $4''$BGO relative to that of the $2''$BGO is important. For $E_\gamma = 1.27$ MeV, the observed ratio is $K = 118 \pm 7$; GEANT leads to $K = 123 \pm 5$.

3.2 Effective beam energy

For the determination of the effective beam energy, E_{eff}, associated with the observed capture γ-ray yield, the beam energy at the center of the target chamber must be known to high accuracy. The determination requires a knowledge of the incident projectile energy, and its energy loss in the gas-target system and target chamber (to its center). These features were tested via the narrow $J^\pi = 2^+$ resonance in ^{4}He(^{12}C,γ_0)^{16}O at $E_R = 2.68$ MeV ($\Gamma_R = 0.62$ keV, $E_\gamma = 9.85$ MeV). With $l_{eff\gamma}(4''\text{BGO}) = 13.0 \pm 0.5$ cm and energy loss values from TRIM [18] (with an assumed 10% uncertainty), the effective target thickness is expected to be $\Delta E = 60 \pm 6$ keV corresponding to a thick-target condition for this resonance. Thus, the observed resonance energy should correspond to the center of the target chamber and be visible as the centroid of the thick-target excitation function. The results for the $4''$BGO (Fig. 4a) led to $\Delta E = 61.2$ keV corresponding to $l_{eff\gamma}(4''\text{BGO}) = 13.2 \pm 1.3$ cm, in good agreement with the value quoted above. Furthermore, the centroid of the excitation function corresponds to E_R if the projectile energy is corrected for its energy loss up to the center of the target chamber: the data led to $z = 102 \pm 11$ mm, which can be compared with the geometrical length $z = 108 \pm 3$ mm (Sect. 2). The data for the $2''$BGO – placed in close

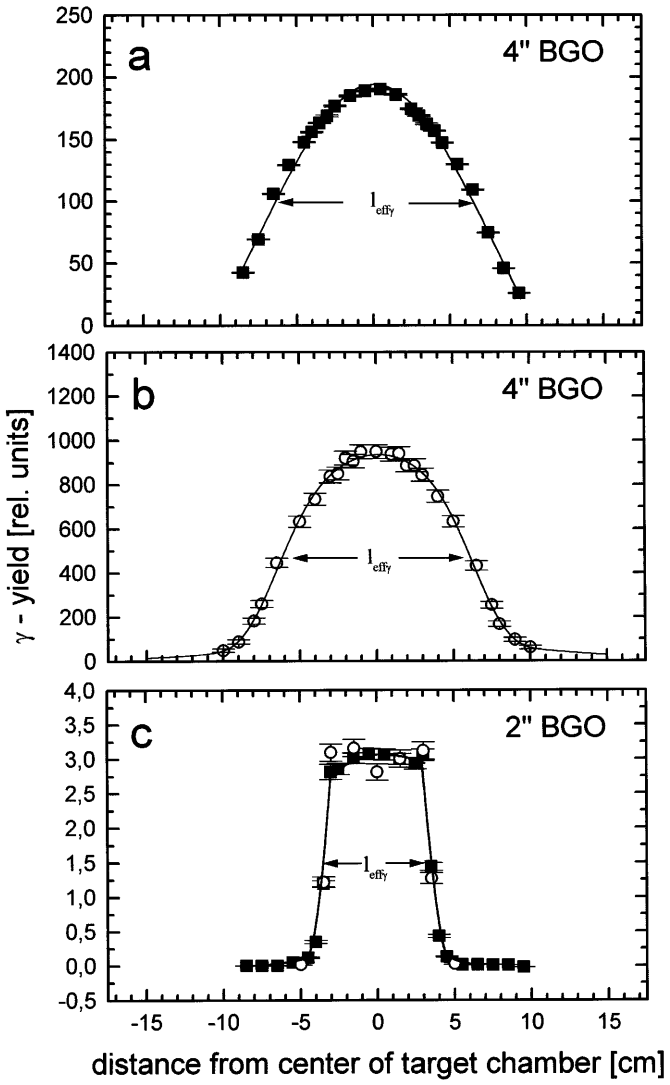

Fig. 3. Response function of a 1.27 MeV γ-ray source as a function of distance from the center of the target chamber for (a) the $4''$BGO and (c) the $2''$BGO. GEANT simulations for the $4''$BGO crystal are shown in (b) and those for the $2''$BGO crystal are indicated as open points in (c)

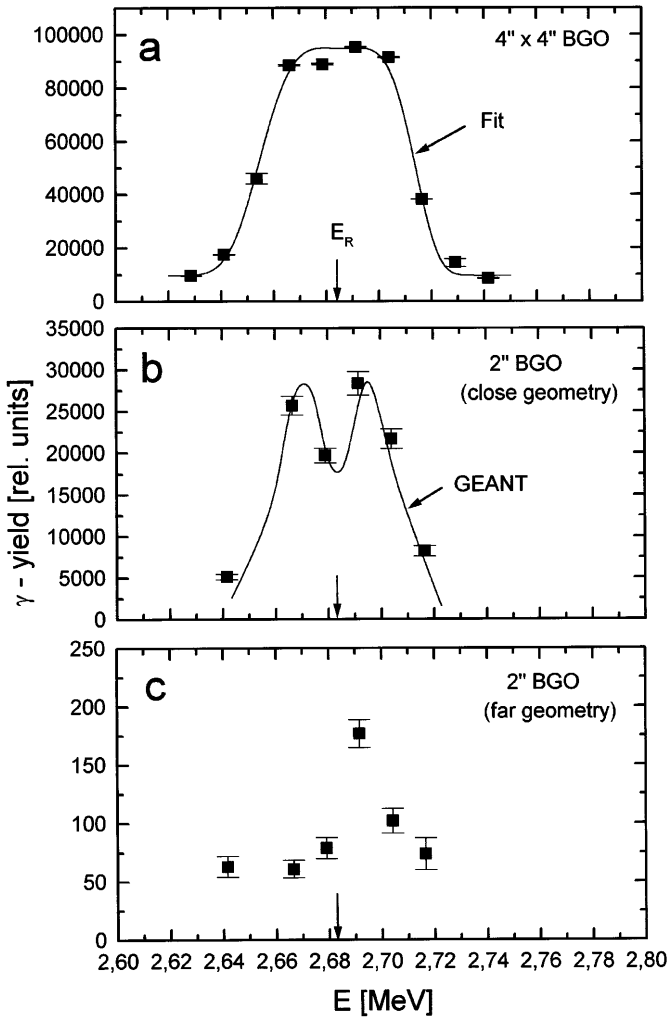

Fig. 4. Thick-target excitation functions at the $E_R = 2.68$ MeV resonance of $^4He(^{12}C,\gamma_0)^{16}O$ ($E_\gamma = 9.85$ MeV) for (a) the 4″BGO in close geometry, (b) the 2″BGO crystal in close geometry, and (c) the 2″BGO in far geometry. The curves represent in (a) a fit leading to a width $\Delta E = 61.2$ keV and in (b) the results of GEANT

geometry ($d_\gamma = 1.5$ cm) – exhibits (Fig. 4b) a symmetric pattern around E_R due to the $W_{E2}(\theta_\gamma) \propto \sin^2\theta_\gamma \cos^2\theta_\gamma$ angular distribution of the resonant (γ_0–ray transition; the pattern is well reproduced by GEANT.

The effective beam energy was determined in two steps. In the first step, the energy at the center of the target chamber, E_c, was calculated from the incident projectile energy and the energy loss over the distance $z = 108$ mm. In the second step, the effective energy $E_{eff} \equiv E$ was determined [1] by the centroid of the cross section area between the energies $E_c + 0.5\Delta E$ and $E_c - 0.5\Delta E$ ($\Delta E =$ energy loss over the length $l_{eff\gamma}$), where the cross section change over the small energy range ΔE was derived from previous work [5].

3.3 Suppression of $E2$ radiation in the 2″BGO

For a point detector, the narrow $J^\pi = 2^+$ resonance in $^4He(^{12}C,\gamma_0)^{16}O$ at $E_R = 2.68$ MeV should not be visible in the γ_0 capture transition at $\theta_\gamma = 90°$. Indeed, the data for the 2″BGO in its usual far geometry ($d_\gamma = 24.5$ cm) reveal (Fig. 4c) a very weak presence of this resonance, with an asymmetry around E_R. This asymmetry is not understood: it may indicate interference effects between the resonant amplitude and a non-resonant amplitude [20] (Sect. 5). GEANT led to a suppression of $E2$ radiation in the 2″BGO by a factor 15, in good agreement with observation (about a factor 14, Fig. 4). Thus, the 2″BGO observes predominantly $E1$ radiation, while the $E2$ radiation makes only a small contribution to the observed γ_0-ray yield (7% for equal cross sections of $E1$ and $E2$ multipoles, $\sigma_{E1} = \sigma_{E2}$).

3.4 Normalization of γ_0 excitation functions

For the normalization of γ_0 excitation functions, the relative number of projectiles was monitored through the observation of the elastic-scattering yield of the ^4He recoils at $\theta_{lab} = 45°$ and $75°$ in Si detectors. In order to determine the deviations of the elastic-scattering yields from the Rutherford scattering law, Ar gas (1 Torr) was admixed into He gas (6 Torr). Since the height of the Coulomb barrier for the $^{12}C + ^{40}Ar$ system is 19 MeV, the system should follow the Rutherford scattering law at $E_{lab}(^{12}C) \leq 15$ MeV and forward angles. The observed energy dependence of the $^{12}C+^4He$ elastic-scattering yields relative to argon, for the beam energies at the center of the target chamber, is shown in Fig. 5. The results have been normalized to Rutherford scattering at the lowest energies, where the intensity ratio approached a constant value. The data are in good agreement with previous work [3,9]. The observed deviations from the Rutherford scattering law are small at most energies and the normalization of the γ-ray data was corrected for these deviations.

3.5 Gamma-ray background

In the $^4He(^{12}C,\gamma_0)^{16}O$ studies, the BGO spectra exhibited a background [14] extending up to the energy region of the γ_0 capture transition; the background increased steeply with ^{12}C beam energy, in particular above the $E_R = 2.68$ MeV narrow resonance, i.e., for $E_{lab}(^{12}C) \geq 10$ MeV. The spectra obtained with the Si detectors showed – at all ^{12}C energies – only the ^4He recoil peak from the $^{12}C+^4He$ elastic-scattering system: no measurable traces of contaminant target gases or of contaminant ion beams could be detected, thus excluding them as the source of the observed background. However, at $E_{lab}(^{12}C) \geq 10$ MeV the $^{12}C + ^{12}C$ fusion reactions have a cross section which is more than a factor 10^6 higher than that of $^4He(^{12}C,\gamma_0)^{16}O$. If the intense ^{12}C beam impinges on beam-defining apertures or the beam stop, a ^{12}C target is built up in a short time, initiating the

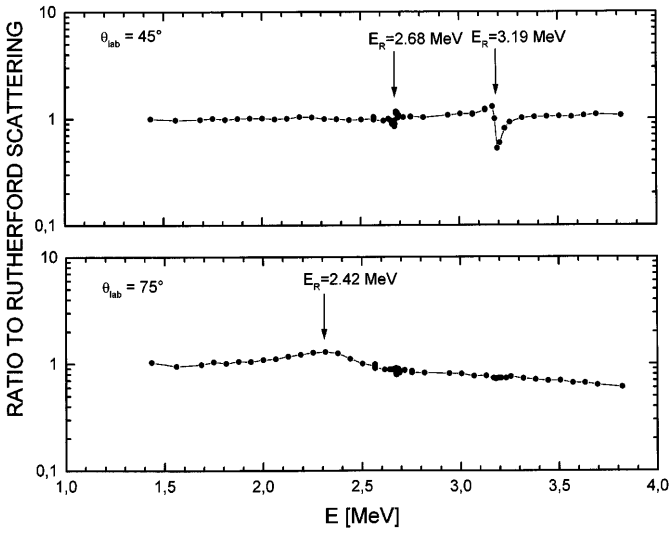

Fig. 5. Energy dependence of the elastic-scattering yield for the $^{12}C + {}^{4}He$ system relative to the Rutherford scattering law at $\theta_{lab} = 45°$ and 75°. The lines through the data points are to guide the eye only

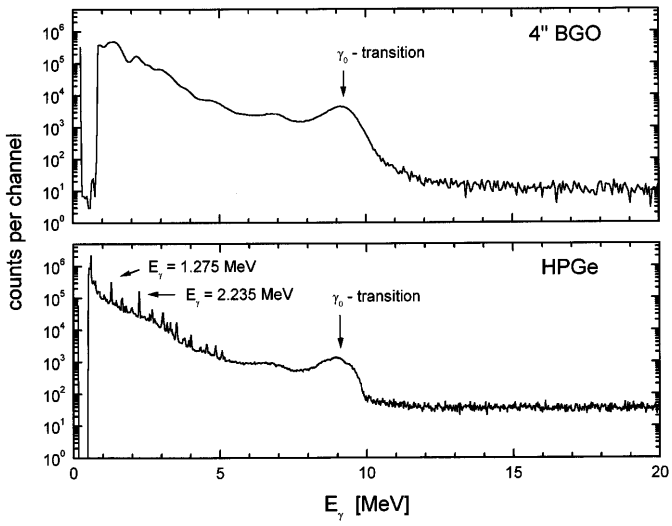

Fig. 6. Spectra of the 4″BGO crystal and 100% HPGe detector (both in close geometry) obtained concurrently at $E = 2.39$ MeV. At energies above and below the γ_0 capture transition in $^{4}He(^{12}C,\gamma)^{16}O$ the spectra are dominated by cosmic and beam-induced background, respectively

$^{12}C + {}^{12}C$ fusion reactions, e.g., $^{12}C(^{12}C,n)^{23}Mg$. To minimize this problem, the gas-target system was built with large apertures and the ion-beam optics was defined by the retractable collimator; furthermore, the shielded Faraday cup was placed in another target hall (Sect. 2). The thermal neutron flux was monitored with a ^{3}He proportional counter placed near the BGO crystals. After optimal beam focusing through the gas-target system (nearly 100% transmission) and after filling the system with ^{4}He gas, the observed neutron flux increased exponentially at $E_{lab}(^{12}C) \geq 10$ MeV [14], consistent with the increase in background observed in the BGO crystals.

Beam-induced γ-ray background from materials such as apertures, or γ rays from thermal neutron capture, should not be Doppler broadened and thus should be visible as relatively narrow peaks in the spectra. However, the poor energy resolution of the BGO crystals did not allow to resolve clearly such narrow peaks from the γ_0 capture transition of $^{4}He(^{12}C,\gamma_0)^{16}O$. To elucidate the situation, the 2″BGO was replaced – in one experiment – by a 100% HPGe detector (close geometry), with an energy resolution of 2 keV at $E_\gamma = 1.33$ MeV. The resulting spectra from the 4″BGO and HPGe (Fig. 6) were obtained at $E = 2.39$ MeV: no narrow peak is visible in the HPGe spectrum above $E_\gamma = 5$ MeV, while the width of the γ_0 capture transition is as broad as for the BGO crystal due to the dominant effect of Doppler broadening. Nearly all narrow lines at $E_\gamma \leq 5$ MeV could be identified: the most prominent $E_\gamma = 2.235$ MeV line arises from the $^{27}Al(\alpha,p)^{30}Si$ reaction initiated by the ^{4}He recoils impinging on the Al material of the target chamber. The identifications were supported by extensive studies [19] using different target gases (H_2, N_2, CO_2, ^{3}He), solid targets (Li, B, C, Al) placed in the target chamber, and an ^{16}O ion beam to study the ^{4}He recoil effects. These studies verified that no significant background is created by the ^{4}He recoils at energies above $E_\gamma = 5$ MeV.

Finally, a spectrum was obtained with a moderated ^{252}Cf neutron source (placed near the BGO crystals) to test the influence of neutrons: a smooth background was observed [14] extending up to about $E_\gamma = 11$ MeV, but no prominent narrow peak was visible above $E_\gamma = 5$ MeV. A nearly identical feature was observed for a 10 MeV ^{12}C beam impinging on a ^{12}C solid target [14]. It was thus concluded that the major source of background arises from local capture of neutrons created in the $^{12}C + {}^{12}C$ fusion reactions and that this background is described by a smooth function without any superimposed narrow lines. The smooth background was taken into account in the analyses of the spectra (Sect. 3.6).

With the passive and active shieldings around the BGO crystals, the cosmic background in the relevant energy range $E_\gamma = 8$ to 11 MeV was reduced by a factor 11 for the 4″BGO and by a factor 25 for the 2″BGO [14].

3.6 Analysis of the BGO spectra

At all ^{12}C beam energies, BGO spectra were obtained with and without ^{4}He gas in the target chamber, in order to observe the prominent beam-induced background. The top part of Fig. 7 shows an overlay of the resulting spectra for the 4″BGO obtained at $E = 2.39$ MeV: the background represents a smoothly varying function of γ-ray energy. The corresponding spectrum of the 2″BGO (no overlay) is shown in the lower part of Fig. 7: its better energy resolution together with the significantly reduced Doppler broadening (far geometry) allowed resolving the full-energy peak from the single-escape peak for the γ_0 capture transition.

For the analysis of the γ_0 capture transition, the line shape for each crystal was derived from the $E_\gamma = 11.67$

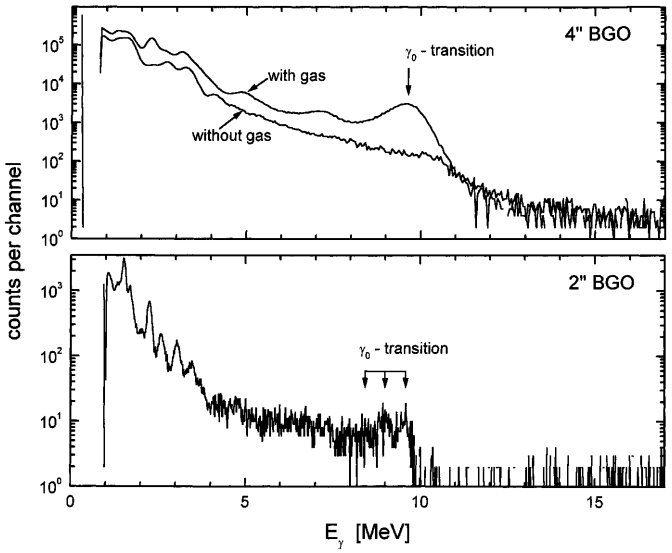

Fig. 7. Spectra obtained with the 2″BGO and 4″BGO at $E = 2.39$ MeV over a running period of 12 hours. The upper part shows – in an overlay – the 4″BGO spectrum obtained without ^{4}He gas over the same length of time

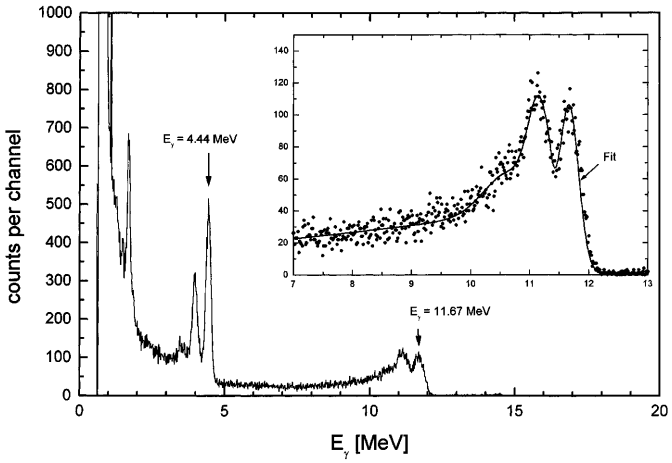

Fig. 8. Spectrum obtained with the 2″BGO at the $E_R = 148$ keV resonance of $^1H(^{11}B,\gamma)^{12}C$. The insert shows the line shape for the $E_\gamma = 11.67$ MeV γ-ray together with a peak-shape fit

MeV γ-ray emitted in the $E_R = 148$ keV resonance of $^1H(^{11}B,\gamma)^{12}C$: the observed spectrum for the 2″BGO is shown in Fig. 8 together with a peak-shape fit including 3 gaussian functions (representing the full-energy peak and escape peaks) and an arctan-function (representing the Compton plateau). It was found from GEANT that the shape of the γ-ray spectrum does not change significantly from that of the 11.67 MeV γ-ray in the relevant energy region $E_\gamma = 8$ to 11 MeV, since the line width is determined predominantly by the Doppler broadening. Thus, the 11.67 MeV line shape was shifted to the appropriate energy given by the beam energy, Q-value, and energy loss, where the height of the line-shape was a free parameter. An energy-independent background from cosmic

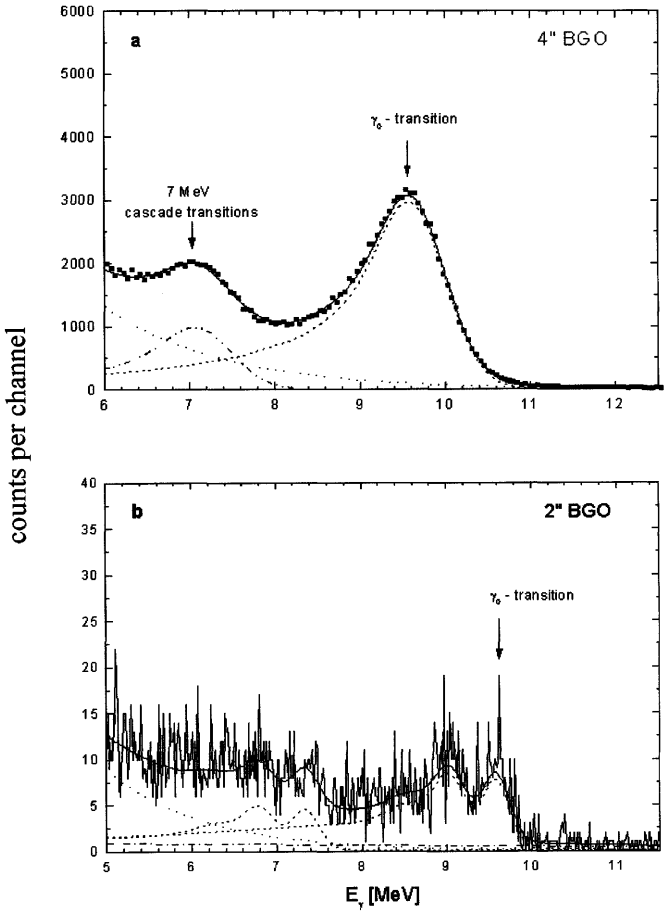

Fig. 9. Relevant section of the spectra obtained with the 2″BGO and 4″BGO at $E = 2.39$ MeV together with their line-shape analyses: dotted curves = γ_0 and 7 MeV cascade transitions, dashed curve = beam-induced background, dash-dotted curve = constant cosmic background, solid curve = sum of these contributions

radiation, an exponential function for the beam-induced background, and an additional line at about 7 MeV (due to cascade transitions) were included in the final analyses of the BGO spectra. Examples illustrating these analyses for both BGO crystals are shown in Fig. 9 for $E = 2.39$ MeV. In all analyses, the same energy region of the γ_0 capture spectrum was used: from the energy just above the full-energy peak to an energy lower by 1.56 MeV. For example, the ratio of counts for the γ_0 capture transition between the 4″BGO and 2″BGO is found to be $K = 117 \pm 1$ (weighted average of 3 independent measurements).

4 Results

4.1 S(E) factor for $E1$ radiation

Due to the far geometry of the 2″BGO, the observation of the γ_0 capture transition was limited at low energies down to $E = 1.69$ MeV, where the running time was 2 weeks, and at high energies up to $E = 3.29$ MeV for similar

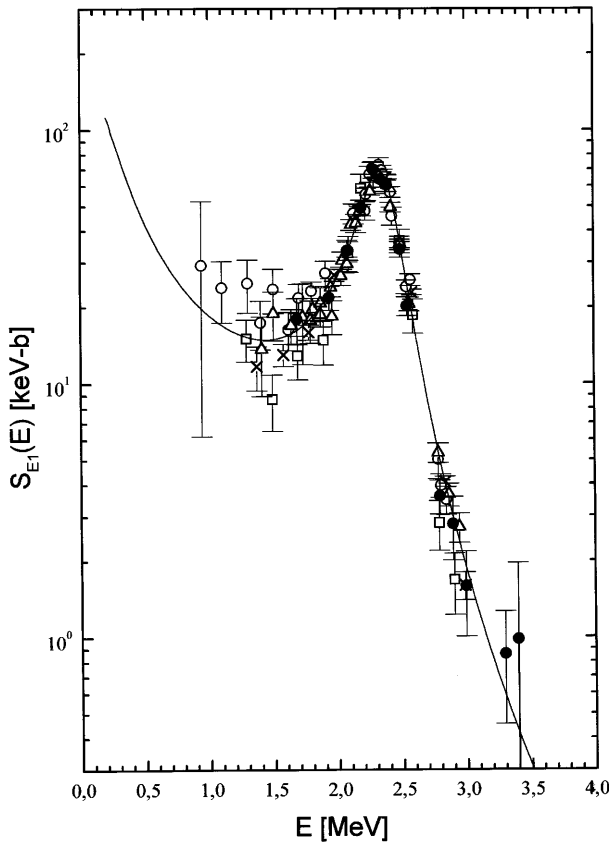

Fig. 10. Summary of available $E1$ data from previous and present work in form of the astrophysical $S(E)$ factor: △ = Dyer and Barnes [3], ○ = Redder at al. [5], □ = Kremer et al. [6], × = Ouellet et al. [7], • = present work. The solid curve represents the reported R-matrix fit [10]

reasons. The number of counts from the γ_0 capture transition was corrected for variation in detection efficiency (GEANT) and normalized to the elastic-scattering yield (Sect. 3.4). The resulting excitation function represents in good approximation data for the $E1$ radiation (Sect. 3.3). After transformation to relative values for the astrophysical $S(E)$ factor, the data were normalized to the absolute $S_{E1}(E)$ values reported near the maximum of the 2.42 MeV resonance [3,5–7]. The results are illustrated in Fig. 10 (and given numerically in Table 1) together with previous $E1$ data: good agreement is noted. The R-matrix fit [10] to previous $E1$ data (solid curve in Fig. 10) led to 79 ± 21 keV-b, which remains essentially unchanged by the addition of the present data. A fit to the present data alone leads [14] to $S_{E1}(E_0) = 95 \pm 44$ keV-b.

4.2 Excitation function in close geometry (4″BGO)

Due to the close geometry of the 4″BGO, the observation of the γ_0 capture transition was possible over the energy range $E = 0.94$ to 3.39 MeV, where for the lowest energy point the running time was 4 weeks. The number of counts from the γ_0 capture transition was corrected for variation in detection efficiency (GEANT) and normalized to the elastic-scattering yield (for other corrections: see below) leading to the yield $I_{\gamma_0}(4''\text{BGO})$. The resulting excitation function (in relative units) is displayed in Fig. 11 and numerical values are given in Table 1. The results are compared with previous data (using a $4 \times 4''$ NaI crystal in close geometry [4]) normalized at the yield maximum of the 2.42 MeV resonance: fair agreement is noted, except at energies near and above 3 MeV, where the present data show a nearly constant yield curve. Note that the comparison appears justified due to similar effective target lengths $l_{eff\gamma}$ and identical detector sizes. A comparison with other angle-integrated data [3,6] is not possible due to lack of primary data.

Table 1. Results for the γ_0 capture transition in ^{4}He(^{12}C, γ)^{16}O

E^a (MeV)	$S_{E1}{}^b$ (keV-b)	$I_{\gamma_0}(4''\text{BGO})^c$ (relative units)	$\sigma_{E2}/\sigma_{E1}{}^d$
0.935		0.51±0.16	0.86±0.70
1.060		1.78±0.34	1.42±0.58
1.185		3.82±0.51	1.13±0.40
1.311		5.74±0.56	0.33±0.21
1.437		11.8±1.0	0.41±0.22
1.562		19.3±1.2	0.20±0.15
1.688	17.9±3.7	33.4±0.4	0.12±0.10
1.940	21.8±2.4	108±1	0.04±0.08
2.091	33.4±2.8	245±2	0.01±0.08
2.191	49.3±3.5	445±3	0.01±0.07
2.291	69.7±5.3	785±4	0.03±0.25
2.340	63.8±4.4	917±5	0.03±0.03
2.390	60.6±3.5	973±4	0.04±0.04
2.441		933±11	0.13±0.07
2.492	33.9±2.4	737±5	0.08±0.06
2.543	20.2±1.7	589±5	0.09±0.08
2.743		356±5	0.72±0.15
2.793	3.6±0.5	263±13	0.44±0.16
2.818		273±5	0.67±0.19
2.893	2.8±0.8	250±20	0.95±0.17
2.943		247±5	1.25±0.22
2.993	1.6±0.6	234±26	1.36±0.20
3.219		200±6	2.46±1.20
3.294	0.9±0.4	287±4	2.91±0.41
3.394		235±32	4.37±0.56

[a] Effective energy
[b] Normalized to previous data near the $E_R = 2.42$ MeV resonance. The quoted uncertainties represent statistical errors only
[c] Statistical errors only
[d] With (1), the quoted uncertainties include the statistical errors in $I_{\gamma_0}(4''\text{BGO})$ (column 3), the errors in the terms $W_i(Ej)$ (Sect. 4.3), and the error in the normalisation ratio $K = I_{\gamma_0}(4''\text{BGO}) \,/\, I_{\gamma_0}(2''\text{BGO})$ at $E = 2.39$ MeV (Sect. 4.3)

4.3 Cross section ratio σ_{E2}/σ_{E1}

Due to its geometry, the 4″BGO sees essentially the sum of the $E1$ and $E2$ multipoles, and interference effects be-

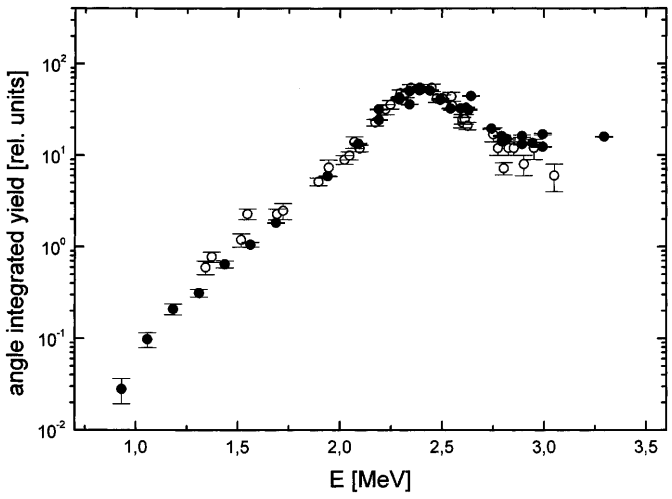

Fig. 11. Excitation function (in relative units) of $^4He(^{12}C,\gamma_0)^{16}O$ as obtained with the 4″BGO in close geometry (•) is compared with results from previous work (○ = Kettner et al. [4], 4″ NaI in close geometry)

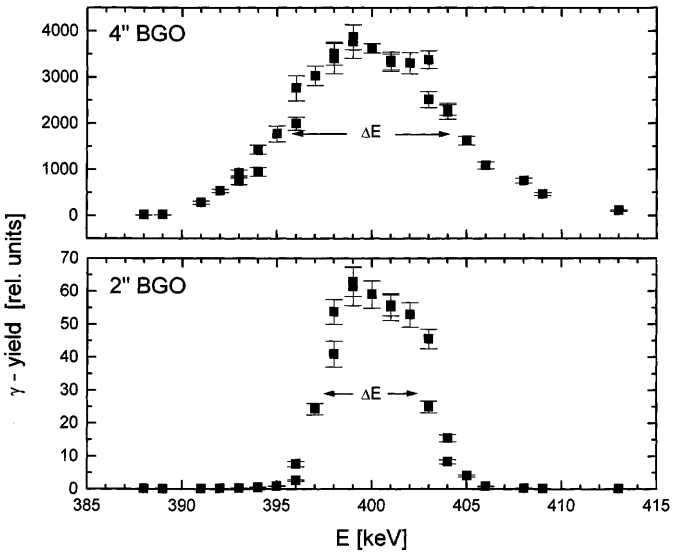

Fig. 12. Excitation function of the 4.44 MeV radiation emitted in the narrow $E_R = 402$ keV resonance of $^1H(^{15}N,\alpha\gamma)^{12}C$ (H_2 gas pressure = 4.0 Torr) as obtained with the 4″BGO and 2″BGO

tween the multipoles are approximately absent at $\theta_\gamma = 90°$ (see below). At a given energy E, the ratio K of the number of counts from the γ_0 capture transition observed by the 4″BGO and the 2″BGO was obtained. This ratio is described by the expression

$$K = (\sigma_{E1}W_{4''}(E1) + \sigma_{E2}W_{4''}(E2)) / (\sigma_{E1}W_{2''}(E1) + \sigma_{E2}W_{2''}(E2)),$$

where $W_{4''}(E1)$ and $W_{4''}(E2)$ are the respective $E1$ and $E2$ angular distributions seen by the 4″BGO, and $W_{2''}(E1)$ and $W_{2''}(E2)$ are those seen by the 2″BGO. From the equation one arrives at the ratio of cross sections σ_{E2}/σ_{E1} between the $E2$ and $E1$ multipoles:

$$\sigma_{E2}/\sigma_{E1} = (KW_{2''}(E1) - W_{4''}(E1) / (W_{4''}(E2) - KW_{2''}(E2)). \quad (1)$$

Note that the terms $W_i(Ej)$ for angular distributions contain also the efficiencies and solid angles of the BGO crystals, which need to be known with high accuracy since the subtractions in the nominator and denominator of equation 1 involve values of similar order. The terms $W_i(Ej)$ were obtained from GEANT. In using GEANT, one must however distinguish between a non-resonant yield and a yield arising from a narrow resonance. In the first case, the γ-ray source is randomly distributed along the beam axis in front of the crystals (random vertex), while in the second case the γ-ray source is located at a fixed point on the beam axis (fixed vertex). For a point target, the influence of the finite solid angle of a detector is taken into account by the use of attenuation coefficients Q_k in the Legendre polynomial expansion of angular distributions. For a random vertex, this procedure cannot be applied. Consequently, GEANT simulations containing the known angular distribution patterns have been performed for both kinds of vertices.

The quality of the simulations was tested using the 4.44 MeV radiation emitted in the narrow $E_R = 402$ keV resonance of $^1H(^{15}N,\alpha\gamma)^{12}C$ (Fig. 12). The known γ-ray angular distribution leads to $W(90°) = 1.15$ for $Q_2 = Q_4 = 1$. At the center of the thick-target excitation functions (Fig. 12) representing a fixed vertex, GEANT predicts the intensity ratio between the 4″BGO and 2″BGO to be $K = 60.5$, in agreement with the observed value 61.4 ± 0.3. For an isotropic angular distribution, the expected ratio is 71.8. If the observed excitation functions are integrated representing the case of a random vertex, the observed ratio is $K = 106 \pm 2$, in good agreement with the GEANT prediction $K = 107.8$.

For the present $^4He(^{12}C,\gamma_0)^{16}O$ studies (random vertex), GEANT leads for the 4″BGO to the expressions $W_{4''}(E1) = -11150E_g^* + 393990$ and $W_{4''}(E2) = -11300E_g^* + 332890$ (both with an uncertainty $< 0.5\%$), and for the 2″BGO to the expressions $W_{2''}(E1) = -175E_g^* + 3560$ (uncertainty $< 1.3\%$) and $W_{2''}(E2) = -18.7E_g^* + 160$ (uncertainty $< 4.6\%$), where $E_g^* = E_{\gamma_0} - 9.561$ and E_{γ_0} in MeV.

In arriving at (1), interference effects between the $E1$ and $E2$ multipoles were assumed to be negligible. This assumption is justified if the cross section does not change significantly over the energy region associated with the effective target length $l_{eff\gamma}$. It is known from previous work [5,7] that the γ_0 angular distributions are asymmetric around 90° at energies outside the $E_R = 2.42$ MeV resonance and forward peaked at energies below this resonance. The latter feature together with the decreasing cross section along $l_{eff\gamma}$ leads to an enhanced observation of the γ_0-flux from the upstream part of the target chamber compared to that from the downstream part. The effect is expected to be stronger for the 4″BGO than for the 2″BGO. The effect was calculated with GEANT, where

the random vertex was weighted according to the energy dependence of the expected cross section and the known γ_0 angular distributions. At $E = 1$ MeV one finds a 15% increase in γ_0-ray flux compared to the unweighted case, which diminishes at energies near the $E_R = 2.42$ MeV resonance. A correction factor, which was linearly interpolated between both energies, was applied in the analyses. For the 2″BGO, the effect was negligible, as expected. Similarly, the observed γ_0-ray energies in the 4″BGO are shifted to higher energies by the Doppler effect, which was also taken into account in the analyses. Finally, the $E_R = 2.42$ MeV resonance decays through cascade transitions via the $E_x = 6.92$ and 7.12 MeV states, which contribute to the observed γ_0-ray yield of the 4″BGO due to summing effects. The data were corrected for these effects using the reported branching ratios [5] and the summing probability (3.8%) from GEANT. For example, the intensity ratio $K = I_{\gamma_0}(4''\text{BGO}) \,/\, I_{\gamma_0}(2''\text{BGO}) = 117 \pm 1$ at $E = 2.39$ MeV (Sect. 3.6) reduces to $K = 113 \pm 1$ due to the summing effects in the 4″BGO; GEANT leads to $K = 111$.

The intensity $I_{\gamma_0}(4''\text{BGO})$, as a function of energy for $E = 0.94$ to 3.39 MeV, was derived from the yield observed with the 4″BGO and corrected for the effects just discussed. In comparison, the intensity $I_{\gamma_0}(2''\text{BGO})$ was limited in energy range, $E = 1.69$ to 3.29 MeV. Since the data from the 2″BGO are well described by the $E1$ capture amplitude, we have adopted the solid curve in Fig. 10 for $S_{E1}(E)$, where the corresponding cross section $\sigma_{E1}(E)$ is proportional to $I_{\gamma_0}(2''\text{BGO})$ at a given E. Finally, the proportionality constant was determined at $E = 2.39$ using the observed ratio $K = I_{\gamma_0}(4''\text{BGO}) \,/\, I_{\gamma_0}(2''\text{BGO}) = 113$. The resulting ratios $K(E)$ together with the terms $W_i(Ej, E))$ (see above) lead to cross-section ratios $\sigma_{E2}(E)/\sigma_{E1}(E)$ using (1). The results are summarized in Table 1: they illustrate the significantly larger uncertainties, e.g. compared to $I_{\gamma_0}(4''\text{BGO})$, due to the subtractions in the nominator and denominator of (1). The results are compared in Fig. 13 with previous data [3,5,7]: within experimental uncertainties the overall agreement is good. The data indicate that at E_0 the $E2$ multipole is as important as the $E1$ multipole, as suggested previously [4] (solid curve in Fig. 13).

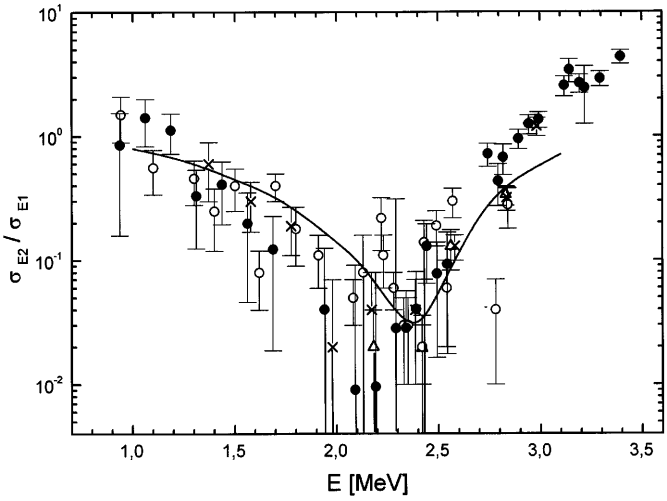

Fig. 13. Cross section ratio σ_{E2}/σ_{E1} as function of energy: △ = Dyer and Barnes [3], ○ = Redder at al. [5], × = Ouellet et al. [7], • = present work. The solid curve represents the ratio inferred previously from the analysis of angle-integrated data [4]

5 Discussion

If $\sigma_{E1}(E)$ is known with high accuracy, one can deduce $\sigma_{E2}(E)$ from the cross-section ratio $\sigma_{E2}(E)/\sigma_{E1}(E)$. In turn, the parametrisation of $\sigma_{E2}(E)$ – using the R-matrix or Breit-Wigner formalisms – should include the $J^\pi = 2^+$ resonances at $E_R = -245$, 2683, and 4358 keV and the direct-capture process into the ^{16}O ground state. Furthermore, the analyses must consider interference terms between the resonances as well as between the direct-capture process and the resonances. However, neither $\sigma_{E1}(E)$ nor $\sigma_{E2}(E)/\sigma_{E1}(E)$ are presently known with sufficient precision and accuracy to arrive at a reliable extrapolated value for $S_{\gamma_0}(E_0)$. The full simulation of our experiment using GEANT together with a preliminary parametrisation of $\sigma_{E2}(E)/\sigma_{E1}(E)$, or equivalently of $\sigma_{E2}(E)$, provided [14] important information for improved analyses of previous data or future experimental efforts. These and other experimental aspects are discussed below.

Our analysis of $\sigma_{E2}(E)$ at energies near the narrow $E_R = 2.68$ MeV resonance indicates significant interference effects between the resonance amplitude and the non-resonant amplitude, even if thick targets ($\Delta E \gg \Gamma$) are used. If the data are not corrected for these effects, one may arrive at incorrect values for the non-resonant amplitude near the resonance. The large scatter of data points near the $E_R = 2.68$ MeV resonance (Fig. 13) might be caused by these effects. It should also be pointed out that these data points are quoted often with small uncertainties (much smaller than data points e.g. at energies below the 2.42 MeV resonance) and thus they dominate any analysis based on χ^2 evaluations. The latter feature applies to all data ($E1$ and $E2$): as long as the data points at energies e.g. far below the 2.42 MeV resonance have uncertainties significantly larger than data points at higher energies, they play a minor role in the χ^2 fits. Thus, small systematic errors in the data points at higher energies are crucial.

A close inspection of the available data for the $E1$ multipole (Fig. 10) shows that at energies below and above the $E_R = 2.42$ MeV resonance the various data sets have systematic differences. There are essentially only 3 data sets [5,7 and present], where the $E1$ multipole was observed at $\theta_\gamma = 90°$ in far geometry. The other data sets [3,4,6] were obtained in close geometry observing the sum of $E1$ and $E2$ multipoles and corrected [3,6] for the contribution of the $E2$ multipole, being thus in a way model-dependent. Furthermore, the data sets [4,6] (using an extended gas target) did not include the interference effects between the $E1$ and $E2$ multipoles (Sect. 4.3) and may thus be too high (or too low) at energies far below (or far above) the

2.42 MeV resonance (e.g. Fig. 11); the effects are absent for a solid target [3]. Finally, to arrive at reliable $E1$ data from the summed $E1$ and $E2$ yields [6] using an expression similar to (1), the angular distributions $W(E1, E)$ and $W(E2, E)$ for an extended γ-ray source must be known with high precision, as discussed in Sect. 4.3. If only the measurements in far geometry are considered, the scatter of data points (Fig. 10) is significantly reduced. Additional data obtained at $\theta_\gamma = 90°$ (in far geometry) over a wide range of energies (with a precision of at least 10%) appear thus highly desirable, which may be obtained with an array of detectors placed in a plane (perpendicular to the beam axis) around the target; such measurements are presently in progress at Bochum. Note that measurements above $E = 3.0$ MeV are as important as low-energy measurements, because they fix the $E1$ background amplitude. However, such measurements are hampered by the background due to the $^{13}C(\alpha,n)^{16}O$ reaction (normal kinematics, [2,3,5,7]) or due to the $^{12}C + ^{12}C$ fusion reactions (inverse kinematics, Sect. 3.5). In the inverse kinematics, one could observe the γ_0 capture transitions in coincidence with the ^{16}O recoils (using a recoil separator, e.g. [6]), which can emerge from a windowless gas target. Since there is always a charge state representing about 50% of all the ^{16}O recoils produced, such coincidence measurements would have a reduction in γ-ray efficiency of only 50% but they would essentially eliminate the background radiations.

Improved data for the ratio $\sigma_{E2}(E)/\sigma_{E1}(E)$ (Fig. 13) may be obtained from measurements of angular distributions using a crystal ball. If the crystal ball can be combined with a recoil separator, background-free data could be obtained. Such a setup would also allow clear observation of the cascade transitions via the $E_x = 6.92$ and 7.12 MeV excited states over a wide range of energies. Of particular importance may be the radiative capture into the $J^\pi = 0^+$, $E_x = 6.05$ MeV excited state due to its large α-cluster configuration; no data exist yet for this capture transition.

One may also pose the question, whether the capture into the ^{16}O ground state – aside from $E1$ and $E2$ multipoles – could not also proceed by a monopole ($E0$). In those nuclides, where monopoles have been observed, they were always of the same order as quadrupoles [21]. Since the $E2$ quadrupole plays a non-negligible role in $^4He(^{12}C,\gamma_0)^{16}O$, one may suggest also a non-negligible role of an $E0$ monopole. The existence of such a monopole may be tested experimentally by the observation of the ^{16}O recoils in a recoil separator, i.e. through a comparison of the ^{16}O flux with the $\gamma_0 - ^{16}O$ coincidence flux (corrected for γ_0-ray efficiency).

The observed d-wave phase shifts (Fig. 14, [9]) were analysed in terms of the $E_R = -245$ and 4538 keV resonances together with a background resonance at higher energy. The fit was however low at the high-energy side of the $E_R = 4538$ keV resonance, which can be compensated in part by choosing a small interaction radius. This deficit was also found in a recent analysis [22], which used these d-wave phase shifts together with some reported $E2$ data to arrive at $S_{E2}(E_0)$. However, additional data for the d-wave phase shifts are available [8] up to $E = 7.5$ MeV (Fig. 14), which were ignored in the analyses just discussed. In the overlapping energy region, good agreement is noted between the two data sets [8,9]. We have performed an R-matrix fit including the $J^\pi = 2^+$ resonances at $E_R = -245$, 4358, and 5858 keV. Using an interaction radius of 5.5 fm, the resulting fit (solid curve in Fig. 14) is significantly improved at the high-energy side of the $E_R = 4538$ keV resonance and leads to a reduced α width $\theta_\alpha^2 \approx 0.5$ for the $E_R = -245$ keV subthreshold resonance. In contrast to previous analysis [22], we do not find a best fit for $\theta_\alpha^2 = 0$.

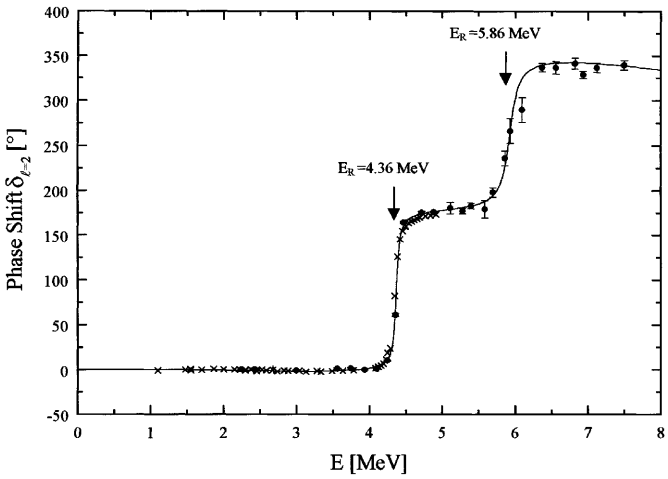

Fig. 14. The observed d-wave phase shift in the $^{12}C + ^4He$ elastic scattering is shown as a function of energy ($\times$ = Plaga et al. [9], $\bullet$ = Agostino et al. [8]), where the curve through the data points is the result of the R-matrix fit

Of course, improved data of elastic scattering, β-delayed α-particles of ^{16}N, and α-transfer reactions will be very helpful to constrain the parameter space of the two subthreshold resonances. There is even the possibility to study $^4He(^{12}C,\gamma_0)^{16}O$ in reverse kinematics (e.g. using an intense γ-ray beam produced in a free-electron-laser facility) or indirectly via the trojan-horse method [23]. Clearly, there exist many novel possibilites and much work remains to be done on all aspects of the problem, before this key reaction of nuclear astrophysics is known with sufficient precision and accuracy.

The authors thank P.Descouvement for the provision of the R-matrix code and for fruitful discussions. We appreciate also comments on the manuscript by R.W. Kavanagh.

References

1. C. Rolfs and W.S. Rodney: Cauldrons in the Cosmos (University of Chicago Press, 1988)
2. R.J. Jaszczak, J.H. Gibbons, R.L. Macklin: Phys. Rev. **C2** (1970) 2452
3. P. Dyer, C.A. Barnes: Nucl. Phys. **A233** (1974) 495

4. K.U. Kettner, H.W. Becker, L. Buchmann, J. Grres, H. Krwinkel, C. Rolfs, P. Schmalbrock, H.P. Trautvetter, A. Vlieks: Z. Phys. **A308** (1982) 73
5. A. Redder, H.W. Becker, C. Rolfs, H.P. Trautvetter, T.R. Donoghue, T.C. Rinkel, J.W. Hammer, K. Langanke: Nucl. Phys. **A462** (1987) 385
6. R.M. Kremer, C.A. Barnes, K.H. Chang, H.C. Evans, B.W. Filippone, K.H. Hahn, L.W. Mitchell: Phys. Rev. Lett. **60** (1988) 1475
7. J.M.L. Ouellet, M.N. Butler, H.C. Evans, H.W. Lee, J.R. Leslie, J.D. MacArthur, W. McLatchie, H.B. Mak, P. Skensved, J.L. Whitton, X. Zhahao, T.K. Alexander: Phys. Rev. **C54** (1996) 1982
8. M.D. Agostino, I. Massa, A. Uguzzoni, G. Vannini, E. Verondini, A. Vitale: Nuovo Cim. **27** (1975) 1
9. R. Plaga, H.W. Becker, A. Redder, C. Rolfs, H.P. Trautvetter, K. Langanke: Nucl. Phys. **A465** (1987) 291
10. R.E. Azuma, L. Buchmann, F.C. Barker, C.A. Barnes, J.M. D'Auria, M. Dombsky, U. Giessen, K.P. Jackson, J.D. King, R.G. Korteling, P. McNeely, J. Powell, G. Roy, J. Vincent, T.R. Wang, S.S.M. Wong, P.R. Wrean: Phys. Rev. **C50** (1994) 1194
11. Z. Zhao, R.H. Frances, K.S. Lai, S.L. Rugari, M. Gai: Phys. Rev. Lett. **70** (1993) 2066
12. F.D. Becchetti, D. Overway, J. Jänecke, W.W. Jacobs: Nucl. Phys. **A344** (1980) 336
13. C.R. Brune, W.H. Geist, R.W. Kavanagh, K.D. Veal: submitted
14. G. Roters: Thesis, Ruhr-Universität Bochum (1996)
15. H.W. Becker, M. Bahr, M. Berheide, L. Borucki, M. Buschmann, C. Rolfs, G. Roters, S. Schmidt, W.H. Schulte, G.E. Mitchell, J.S. Schweitzer: Z. Phys. **A351** (1995) 453
16. J. Görres, K.U. Kettner, H. Kräwinkel, C. Rolfs: Nucl. Instr. Meth. **177** (1980) 295
17. CERN library
18. J.P. Biersack, J.F. Ziegler: Transport of ions in matter, TRIM program Version 95.06 (IBM Research, New York, 1995)
19. B. Greiff: Diplomarbeit, Ruhr-Universität Bochum (1995)
20. D. Rogalla: Diplomarbeit, Ruhr-Universität Bochum (1997)
21. P. Kienle: private communication
22. L. Buchmann, R.E. Azuma, C.A. Barnes, J. Humblet, K. Langanke: Phys. Rev. **C54** (1996) 393
23. C. Spitaleri: private communication